

An Ultra Fast Low Power Convolutional Neural Network Image Sensor with Pixel-level Computing

Ruibing Song, *Student Member, IEEE*, Kejie Huang, *Senior Member, IEEE*, Zongsheng Wang, *Student Member, IEEE*, and Haibin Shen

Abstract—The separation of the data capture and analysis in modern vision systems has led to a massive amount of data transfer between the end devices and cloud computers, resulting in long latency, slow response, and high power consumption. Efficient hardware architectures are under focused development to enable Artificial Intelligence (AI) at the resource-limited end sensing devices. This paper proposes a Processing-In-Pixel (PIP) CMOS sensor architecture, which allows convolution operation before the column readout circuit to significantly improve the image reading speed with much lower power consumption. The simulation results show that the proposed architecture enables convolution operation (kernel size=3×3, stride=2, input channel=3, output channel=64) in a 1080P image sensor array with only 22.62 mW power consumption. In other words, the computational efficiency is 4.75 TOPS/w, which is about 3.6 times as higher as the state-of-the-art.

Index Terms—processing-in-pixel, visual perception, convolutional neural network, CMOS image sensor.

I. INTRODUCTION

COMPUTER vision, which trains computers to interpret and understand the visual world, is one of the research hotspots in computer science and Artificial Intelligence (AI). With the rapid development of machine learning technologies, Convolutional Neural Networks (CNNs) have outperformed previous state-of-the-art techniques in computer visions such as object detection [1], face recognition [2], video compression [3], motion transfer [4], etc.

Although CNN has significantly improved visual systems' performance, they consume many operations and storage, making it difficult for end devices to independently complete the computation. Therefore, in modern visual systems, data capture and analysis are separately carried out by sensing devices and cloud computers. The separation of the data capture and analysis has led to a tremendous amount of data transfer between the end devices and the cloud computers, resulting in long delay, slow response, and high power consumption [5]. What's more, in many vision applications, the systems have to work continuously for monitoring or anomaly detection, i.e., surveillance cameras. The low information density has seriously wasted communication bandwidth, data storage, and computing resource in such applications.

K.Huang and H.Shen are with the College of Information Science & Electronic Engineering, Zhejiang University, 38 Zheda Road, Hangzhou, China, 310027, and also with Zhejiang Lab, Building 10, China Artificial Intelligence Town, 1818 Wenyi West Road, Hangzhou City, Zhejiang Province, China, email: huangkejie@zju.edu.cn; shen_hb@zju.edu.cn

R.Song and Z.Wang are with the College of Information Science & Electronic Engineering, Zhejiang University, 38 Zheda Road, Hangzhou, China, 310027, email: songruibing@zju.edu.cn; wangzongsheng@zju.edu.cn

To improve the efficiency of modern vision systems, researchers are focusing on reducing the readout power consumption or data density of sensors [6]–[11]. One of the most promising methods is to move the processing units much closer to the sensing units. Equipping CMOS Image Sensor (CIS) with a neural network processor can be divided into three categories: (1) Processing-Near-Sensor (PNS) with Deep Learning Accelerators (DLA); (2) Processing-In-Sensor (PIS); and (3) Processing-in-Pixel (PIP). The PNS architecture utilizes on-chip DLA to shorten the physical distance between the processor and the image sensor [12]–[14]. The PIS architecture is proposed to reduce the data transfer distance, read operations, and analog-to-digital conversions. For example, Redeye performs several layers of CNN calculation in CIS by additional analog arithmetic circuits before readout, saving 85% energy due to the reduced read operations [15]. However, it needs lots of analog capacitors for data storage, leading to a large area overhead and low computational efficiency. PIP is a fully integrated architecture to enable sensing and computing simultaneously. However, they may only support low-level processing [16] or need complicated pixel circuits, which lead to the excessive area and power consumption [17], [18].

We propose a novel PIP architecture to enable high precision convolutional neural network computation in pixels to address the limitations mentioned above. The multiplication is achieved by pulse modulation during the exposure period. The charge redistribution does the accumulation at the pixel level. The whole pixel array is organized with 3×3 kernels to enable massive parallel convolution operations, generating one complete output feature map in four steps when the stride is two, and the filter size is 3×3×3. Our proposed architecture could also support 60 frames and 1080P computation speed when the output channel size is 64. It only consumes 22.62 mW power and has a computational efficiency up to 4.75 TOPS/w, which is about 2.6 times higher than state-of-the-art. Our proposed splitting technique achieves the realization of other kernel sizes.

This paper is organized as follows: Section II presents the related works. Section III introduces the detailed design of our proposed scheme, including the overview architecture, the pixel circuit, the MAC operation, array convolution, and the implementation of other convolution kernel sizes. Section IV analyzes the simulation results and finally the conclusion is drawn in Section V.

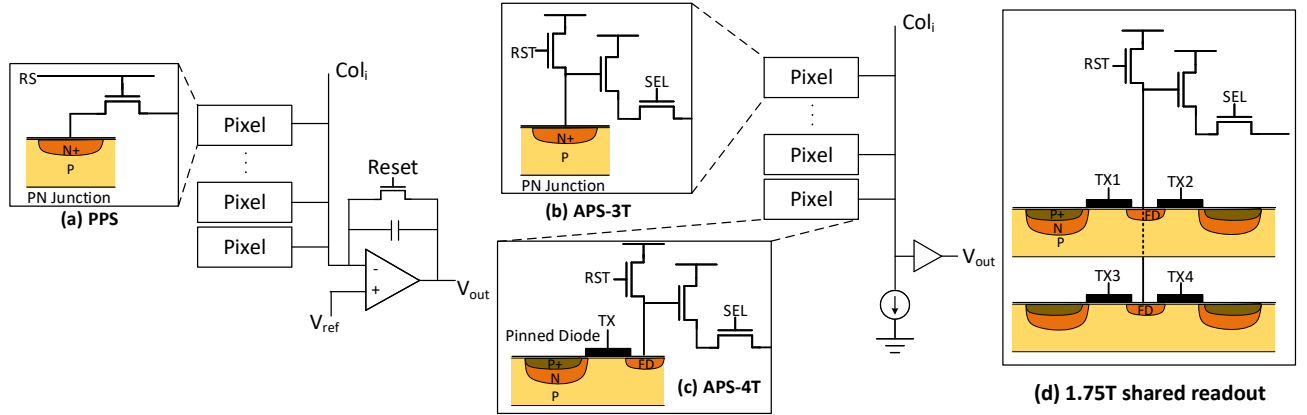


Fig. 1. Four types of CIS pixel circuit: (a) PPS, (b) APS-3T, (c) APS-4T, and (d) APS-1.75T (shared readout circuit).

II. BACKGROUND AND RELATED WORK

A. CMOS Image Sensor

Pixel is the primary component in CIS to convert optical signals into electrical signals by photodiodes. Fig. 1 shows four types of pixel circuits according to [19].

As shown in Fig. 1(a), Passive Pixel Sensor (PPS) is the early mainstream CIS technology, consisting of a photodiode and a row-selection transistor. The output of PPS is a current signal, which is then converted to a voltage signal through the column charge-to-voltage amplifier, and finally quantized by Analog to Digital Converter (ADC). The main advantage of PPS is the small pixel area. However, it suffers from low Signal-to-Noise Ratio (SNR) and low readout speed.

In Active Pixel Sensors (APS), a reset transistor is used to periodically reset the photodiode and a source-follower transistor is employed to buffer and separate the photodiode from the bit line to reduce noise. There are mainly three types of APS, including APS-3T, APS-4T, and APS-1.75T. APS-3T shown in Fig. 1(b) can't solve the kTC noise caused by its reset. As shown in Fig. 1(c), APS-4T (Pinned Photodiode (PPD)) includes a transfer transistor TX and a floating diffusion (FD) node to further reduce the noise by decoupling the reset and the discharge of the photodiode. Besides, the dark current of the P+NP structure is also smaller than that of the PN junction.

However, the PPD structure has four transistors, which significantly reduces the Filling Factor (FF). As a result, the photoelectric conversion efficiency and SNR are reduced. APS-1.75T is then proposed to share the readout and reset transistors, as shown in Fig. 1(d). A total of 7 transistors are shared by four pixels, which highly reduces the area occupied by the readout circuit in each pixel and thus dramatically improves the filling factor.

B. PNS, PIS, and PIP Architectures

To reduce the distance between the data capture and analysis, in sensor or near sensor computing has been widely proposed. Fig. 2 shows the block diagram of different architectures, including traditional architecture, PNS, PIS, and PIP.

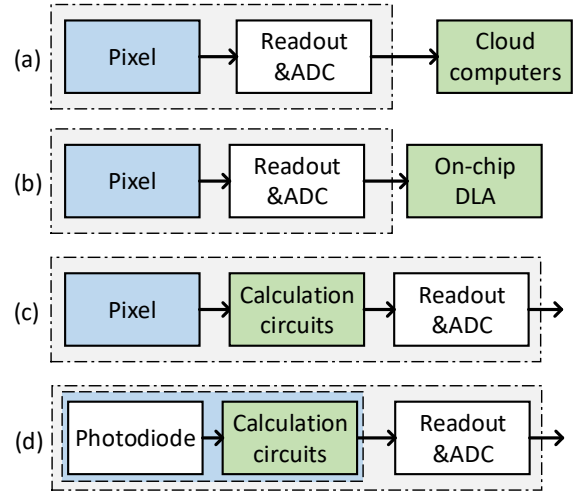


Fig. 2. Different architectures of visual systems. (a) Traditional architecture. (b) PNS architecture. (c) PIS architecture. (d) PIP architecture. Blue boxes represent the pixel, grey boxes mean the sensors, and green boxes show where the calculation is conducted.

PNS architecture (Fig. 2(b)). [12] utilized 3D-stacked column-parallel ADCs and Processing Elements (PEs) to perform spatio-temporal image processing. In [20], the signals are quantized by the ramp ADCs and then computed by the on-chip stochastic-binary convolutional neural network processor. Compared with the traditional architecture shown in Fig. 2(a), PNS architectures reduces the energy consumption of data movement, but the energy consumed by the data readout and quantization is still not optimized.

PIS architecture (Fig. 2(c)). In PIS architectures, the computing units are moved to the place before ADC to reduce quantization frequency. Unlike PNS, the computing in PIS is usually done in the analog domain. In [21], the proposed CIS can realize a maximum 5×5 kernel-readout with a minimum of one slide step for convolution operations. Analog processing units directly process the readout signals without ADCs. In [22], input images are captured in the current mode and trans-

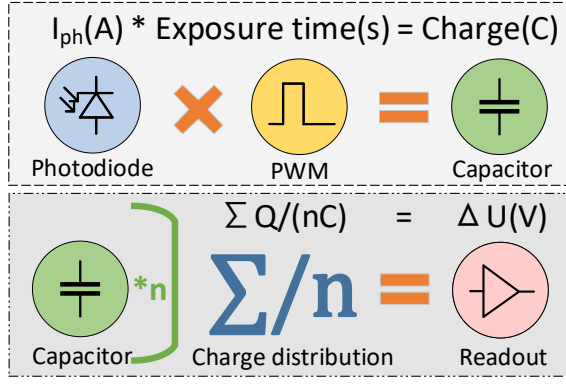


Fig. 4. The calculation flow diagram of the proposed architecture.

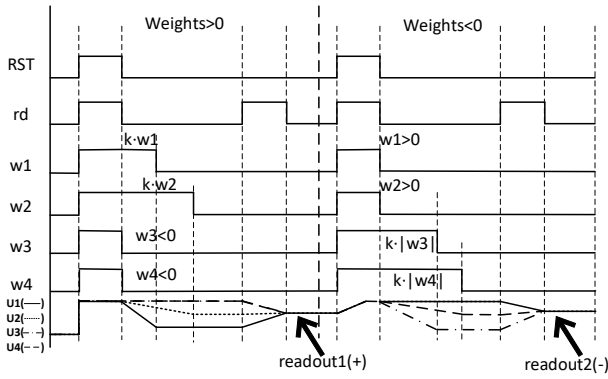


Fig. 5. The convolution sequence diagram of the pixel circuit.

Fig. 4 shows the calculation flow of the MAC operation under the proposed PIP architecture. The multiplication of photocurrent and weights is realized in the pixel unit by controlling the exposure time of photodiodes. The exposure time of photodiodes is modulated by the weights (8 bit) in the convolution kernel. The multiplication results are stored on the capacitors, which can be connected between different pixel units to realize summation by charge redistribution.

The timing diagram is shown in Fig. 5, which only contains four pixels for simplicity. When the signal RST is high, both RST_x and RST_y are asserted to reset the capacitors' potential to Vdd. The exposure stage is started after the reset stage when both RST and rd are de-asserted. In this stage, the control pulses of exposure signals w_1 - w_4 are modulated by the convolution kernel weights. The exposure time T is proportional to the weight value w . Since the photocurrent I_{ph} is unchanged in a short period, the charge Q stored on capacitor C can be expressed as

$$Q = CU_{rst} - It = CU_{rst} - Ikw \quad (1)$$

where k is the exposure constant, adjusted by the software according to the external light intensity. So the charge Q on the capacitor represents the product of the photocurrent I and the corresponding weight value w in the convolution kernel.

After the exposure, it is the charge redistribution and readout stage when rd is asserted. The Convlink line redistributes

the charges stored in the capacitor Q_1 - Q_4 . According to the principle of charge redistribution, the voltage would reach a uniform value of U_{conv} . If only considering the four pixels shown in Fig. 3(a), the value of U_{conv} can be expressed as

$$U_{conv} = \frac{(Q_1 + Q_2 + Q_3 + Q_4)}{C + C + C + C} \quad (2)$$

$$= U_{rst} - \frac{k}{4C}(I_1w_1 + I_2w_2 + I_3w_3 + I_4w_4)$$

where $\frac{k}{4C}$ is a known constant, so the voltage U_{conv} on the Convlink line represents the sum of the four multiplication results, thus achieving MAC operation in-pixel level. Assuming that the convolution kernel size is r^2 , one of the output results of the 1-st layer convolution can be obtained by connecting $4r^2$ such adjacent pixels by the Convlink lines, which can be expressed as

$$U_{conv} = \frac{\sum_{i=1}^{4r^2} Q_i}{4r^2 C} = U_{rst} - \frac{k}{4r^2 C} \sum_{i=1}^{4r^2} [I_i w_i] \quad (3)$$

The weight precision of the convolution kernel used in the system is 8-bit. That is, the weight size of the convolution kernel ranges from -128 to +127. The positive and negative weights of the convolution kernel can be achieved by subtracting two consecutive exposures, as shown in Fig. 5. As w_1 and w_2 are positive, they are enabled in the first exposure period. The negative w_3 and w_4 are enabled in the second exposure period. The readout operation is done after the redistribution. The digital circuits subtract the two readout operations in Fig. 5 after the ADCs, which is expressed as

$$U = U^- - U^+ = \frac{k}{4r^2 C} (\sum [I_i w_i^+] - \sum [I_i w_i^-]) \quad (4)$$

Eq. (4) also illustrates that the Correlation Double Sampling (CDS) is realized because it eliminates the influence of dark current.

B. Convolution Operation in Array

After introducing the basic idea of the convolution operation, this section gives a detailed introduction to the system's overall architecture and the sliding convolution on the entire pixel array.

As can be seen from Fig. 3, the most fundamental component of the pixel array is a pixel unit containing four photocells. Split transistors separate the Convlink wires of the adjacent pixel units. Each column of pixel units includes a column readout circuit and a column ADC outside the array, which can read the convolution results and convert them into digital signals. The adopted ADC is taken from [28], which consumes 4.04 μ W with a 12.5 MS/s sampling rate.

The flow of convolution operation in the array is shown in Fig. 6. In the following example, we assume that the convolution kernel size is 3×3 and the stride is 2. In Fig. 6, each square represents a pixel unit. The dash horizontally and vertically interlaced lines mean to break the split transistors at that position to separate the Convlink wires, while other split

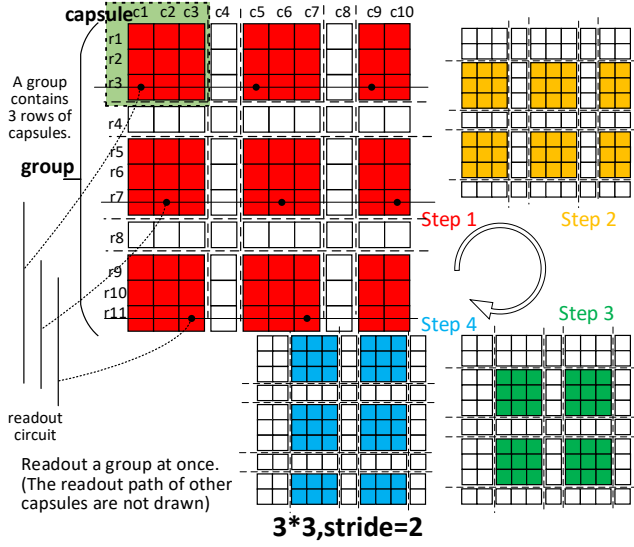


Fig. 6. The flow diagram of the array convolution operation. The convolution kernel size is 3x3, and the stride is 2.

transistors are closed. The 3x3 connected active pixel units are defined as capsules. Then the whole array can be divided into several independent capsules. The Convlink wires connect the pixel units in each capsules. The capsules' exposure and charge redistribution (MAC operations) are enabled simultaneously in each step. We defined the three rows of capsules which are readout simultaneously as a group.

As stated in the previous section, the MAC operation can be achieved by connecting the Convlink wires of all pixel units corresponding to a convolution kernel during computation. More MAC operations should be carried out simultaneously to maximize parallel operation and computing throughput. Because the charge redistribution is a destructive read of pixel values, regions of multiple simultaneous MAC operations must be non-overlap. The non-overlap is achieved by dividing the convolution procedures of the entire array into four steps, as shown in Fig. 6. In each step, the colored squares represent the active pixel units, and the uncolored squares represent pixel units not involved in the computation of this step. To minimize the power consumed by the photodiode reset, RST_y and RST_x disconnect the unpainted pixel from the adjacent unit in the row and column directions, respectively. In such a scenario, all the convolution areas in one step can be calculated and read out with only one exposure. In each step, the active pixel units will achieve the MAC operations with the convolution kernel, and calculate a quarter of the convolution result. After four steps of calculations, a complete convolution operation is finished. As we exposure twice for each step's positive and negative weights, eight exposure cycles are needed for each convolution operation.

The above convolution operation need to carefully plan the hardware wiring. As shown in Fig. 7(a), when the convolution kernel size is 3x3 and stride is 2, pixels in the same row are connected to the wire in the following order: $W_1, W_2, W_3, W_2, W_1, W_2, W_3, \dots$. In this way, each capsule in a step contains the

same wire orders " W_1, W_2, W_3 " in first and second steps and " W_3, W_2, W_1 " in the third and fourth steps. As the minimum cycles of the wire order are 2, so only even stride can be supported.

As each column of pixel units is connected to a column readout circuit, each capsule includes 3 column readout circuits. So the calculation results of every three rows of capsules can be read by the three readout circuits simultaneously. To achieve this readout method, pixels with the row number x ($x = 4n + 3, n = 0, 1, 2, 3, \dots$) are connected to three independent row enabling signals C_1, C_2, C_3 as shown in Fig. 7(b). As shown in Fig. 6, signal C_1 is active in the 3rd row, and signal C_2 is active in the 7th row so that the first row of capsules can be read from the first column of the readout circuit while the second row of capsules from the second column of readout circuit.

The processing sequence of the convolution operation is shown in Fig. 8. The subscript n represents the n^{th} group. As shown in Fig. 8(a), after a readout operation of the n^{th} group is finished, the signal rd_n is de-asserted, rd_{n+1} is asserted for the readout of the $(n+1)^{th}$ group, and rst_n are activated to reset the n^{th} group. As shown in Fig. 8(b), a capsule is reset immediately after each readout operation and then begin the exposure for the next readout. Assuming the resolution is 1080P, the convolution kernel size is 3x3, the stride is 2, and each step contains 270 rows of convolution kernel results, then each step needs 90 readout operations. As shown in Fig. 6, in different steps, the active capsules are corresponding to different pixel units. Since the next readout of the n^{th} group in the next step needs an extra readout cycle's delay to avoid overlapping, so the next readout of a group is separated from the reset by $(90-1)$ readout cycles. Assuming the readout interval is T_{rd} , the number of the readout operations in each step is n_{rd} , the time interval between two readouts of the same capsule is $(n_{rd} - 1)T_{rd}$, the reset interval is T_{rst} , and the maximum exposure time is T_{expo} . As a capsule's reset and exposure stage need to be finished before the next readout operation, there should be

$$(n_{rd} - 1)T_{rd} > T_{rst} + T_{expo} \quad (5)$$

C. Universal Implementation of Convolution Kernel with Different Size

To support other kernel size with the same wires, we propose a method called "kernel splitting" to split the convolution kernel. As shown in Fig. 9(a), two 5x3 convolution kernels k_1 and k_2 are used to form a 5x5 convolution kernel. The kernel k_1 includes the first 3 columns of the 5x5 kernel. k_2 includes the 4-5 columns. A 5x5 convolution operation can be realized by two 5x3 convolution operations, which can use the same wiring method as 3x3 convolution operation. In a 5x3 convolution operation, the difference against a 3x3 convolution operation is that each capsule includes 5x3 pixel units connected by the Convlink wire. Assuming the stride is 2, the number of steps is changed to 6 instead of 4 because each capsule has 5 rows of pixels and need three different steps to avoid overlapping in column direction. For readout

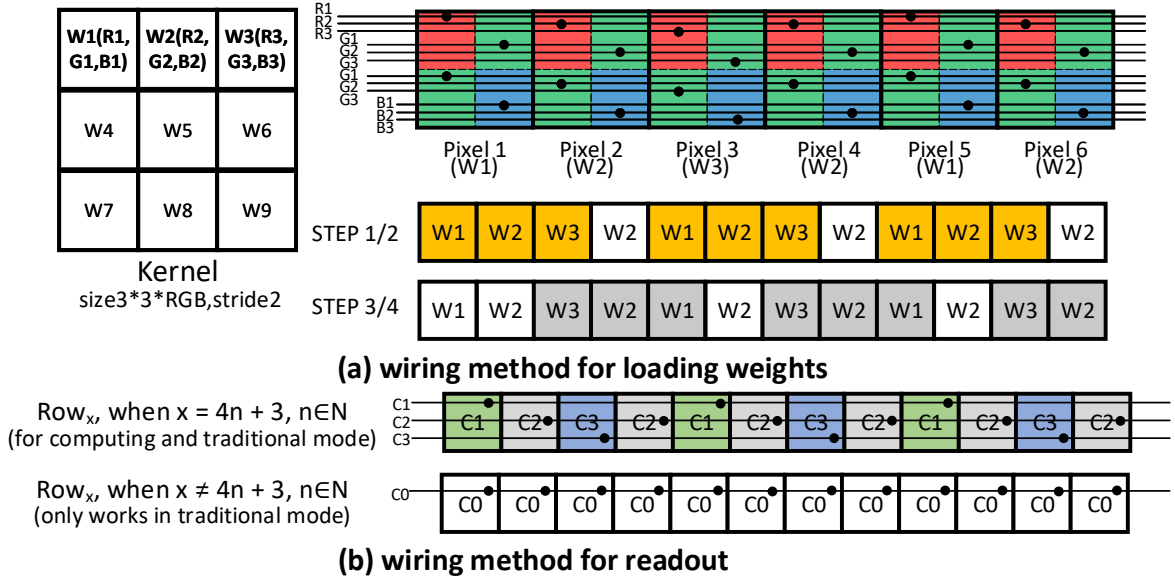


Fig. 7. (a) The wiring way of weight loading. (b) The wiring method for readout. The convolution kernel has a size of 3×3 , and the stride is 2.

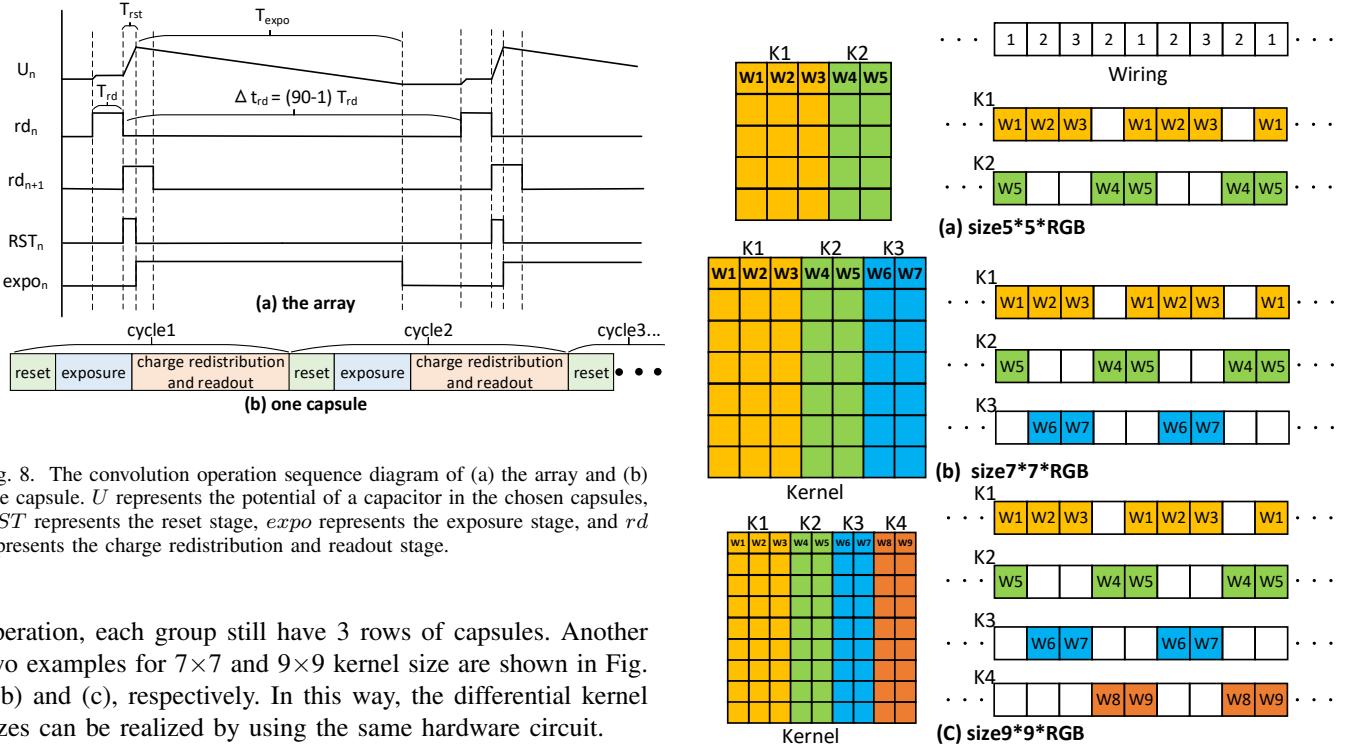


Fig. 8. The convolution operation sequence diagram of (a) the array and (b) one capsule. U represents the potential of a capacitor in the chosen capsules, RST represents the reset stage, $expo$ represents the exposure stage, and rd represents the charge redistribution and readout stage.

operation, each group still have 3 rows of capsules. Another two examples for 7×7 and 9×9 kernel size are shown in Fig. 9(b) and (c), respectively. In this way, the differential kernel sizes can be realized by using the same hardware circuit.

Assuming the kernel size is $r \times r$ and the stride is s , the total number of steps is $\frac{r+1}{s}(r-1)$, where the ratio $\frac{r+1}{s}$ needs to round up to an integer if necessary. For a fixed height of the pixel array H (1080 in our case), the total number of output rows in each step is $\frac{H}{r+1}$. Since each readout operation contains three output rows, the minimum ADC conversion rate can be calculated by

$$f_{ADC(min)} = \frac{2nfH(r-1)}{3s} \quad (6)$$

where f is the frame rate and n is the number of channels.

Fig. 9. The convolution implementations of kernel splitting. The convolution kernel size is (a) 5×5 , (b) 7×7 , and (c) 9×9 .

As each step requires two exposures for the positive and negative weights. The real frame rate f_{real} is defined as the product of frame rate and the output channel number $f \times n$. With a fixed maximum exposure time T_{expo} , the maximum real frame rate can be calculated by

TABLE I
COMPARISON OF DIRECTLY AND SPLITTING CONVOLUTION OPERATION

operation condition	minimum ADC conversion rate	maximum real frame rate
3×3	2.76 MHz	3840
5×5 (splitting)	1.84 MHz	1280
7×7 (splitting)	1.38 MHz	640
9×9 (splitting)	1.11 MHz	384

$$f_{real(max)} = \frac{s}{2(r^2 - 1)T_{expo}} \quad (7)$$

As shown in Eq. (6), the minimum conversion rate of ADC is proportional to the frame rate f , the channel number n , and the kernel size r . It is inversely proportional to the stride s . As shown in Eq. (7), when the kernel size increases, the maximum real frame rate will decrease.

Assuming the resolution is 1080P, the stride is 2, and the maximum exposure time is 32.56 us (calculated when kernel size is 3×3, stride is 2, frame rate is 60, and output channel number is 64), the maximum real frame rate and the minimum ADC conversion rate are calculated for (a) 3×3 kernel size, (b) 5×5 kernel size (splitting), (c) 7×7 kernel size (splitting), and (d) 9×9 kernel size (splitting) and shown in Table I. The calculation of $f_{ADC(min)}$ is based on the calculated $f_{real(max)}$ in each condition. The results shows when kernel size increases, the conversion rate of ADC will decrease. This is because the real frame rate decreases and the readout operation frequency decreases.

D. Traditional Mode and Mode Switch

In the preceding three subsections, we have introduced the realization of convolution operations. In the convolution mode, it does not output the raw image. However, the original image is vital for some applications. The proposed CIS can work in the traditional mode appropriate control signals and output the raw image.

We set the opening time of transistors W_1 - W_4 to a unified length according to the external light intensity to achieve this. During a reading, the RD transistors of four pixels can be selected in turn to read out RGB data. In the pixel array, as each pixel in a column shares the same column readout circuit, each row of pixels will be selected by enabling C_0 or C_1 - C_3 in turn for readout. It needs a total of 4H readout operations to read the entire pixel array and obtain the RGB three-channel image with a size of $H \times W$.

The switch between computing mode and traditional mode can adopt an event-driven mechanism. When the target object is identified in the subsequent computing module results, the CIS control mode can be switched to output the complete raw image in the traditional mode. The light intensity can also determine the exposure time to avoid overexposure or underexposure.

IV. SIMULATION RESULTS

Our proposed architecture was implemented with a generic 45nm CMOS process. To simulate the response of the pho-

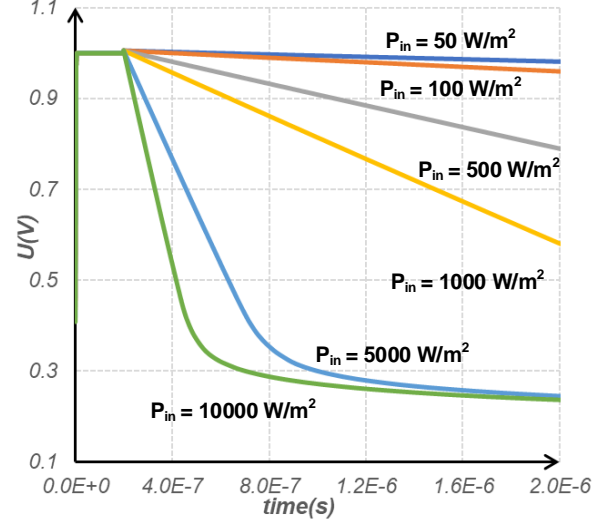


Fig. 10. Simulation result of a single photodiode based on the model given in Eq. (8)-(10).

todode, an analytic model taken from [29] is used in the simulation. The model can be expressed as

$$J_{np} = \frac{qG_L(0)L_p}{1 - (\alpha L_p)^2} [\alpha L_p e^{-\alpha x_j} + \sinh \frac{x_j}{L_p} + A(x_j, L_p) \cosh \frac{x_j}{L_p}] + \frac{qG_L(0)}{\alpha} [1 - e^{-\alpha x_{dr}}] e^{-\alpha x_j} + \frac{qG_L(0)L_n}{(\alpha L_n)^2 - 1} [A(L - x_d, L_n) + \alpha L_n] e^{-\alpha(x_j + x_{dr})} \quad (8)$$

where

$$A(x, y) = \frac{e^{-\alpha x} - \cosh \frac{x}{y}}{\sinh \frac{x}{y}} \quad (9)$$

$$G_L(0) = \alpha \frac{P_{in}}{hc} \lambda \eta (1 - R) \quad (10)$$

Fig. 10 shows the simulation results of the photodiode model in our proposed pixel circuit. Firstly all the capacitors and diode are reset to Vdd (1 V). After exposure with different light intensities, the voltages are declined at different speeds. The results show that the potential should be held above 0.5 V to ensure linearity.

A. Circuit function verification

The transient simulation result to verify the correctness of our proposed pixel circuits' MAC operation is shown in Fig. 11. Signal RST represents both RST_x and RST_y . Different values of P_{in} and weights are set verify multiplication and accumulation.

At 0 us, the reset stage begins after RST, rd, and w_1 - w_4 are asserted to reset the capacitors to 1 V. At t_1 , the exposure stage begins after RST and rd are de-asserted. According to the weights, w_1 - w_4 stay open with exposure time and the voltage on capacitors U_{C1} - U_{C4} are decreased with different speeds determined by the input light power. This stage achieves the

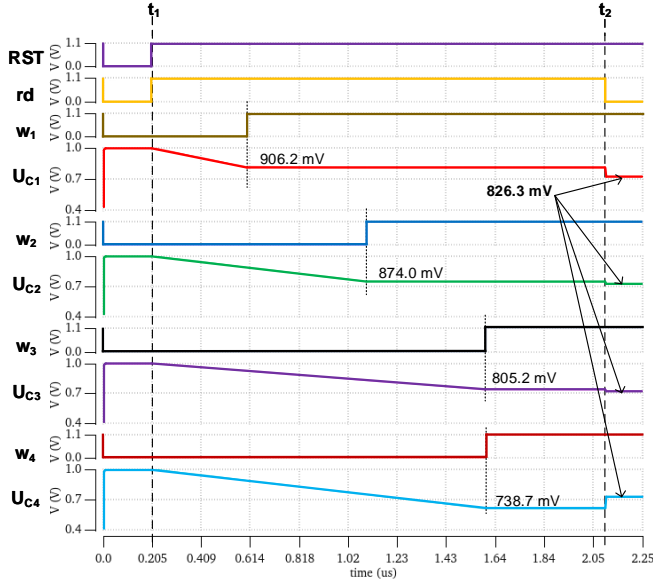


Fig. 11. Simulation result of our proposed pixel circuit.

multiplication operation between the input light power and weights. At t_2 , the charge redistribution and readout stage begins when rd is asserted to redistribute the four capacitors' charge. $U_{C1}-U_{C4}$ reach a unified voltage level in a short time. This stage achieves the average operation. Therefore the MAC operation is achieved after the multiplication in exposure stage and the average in charge redistribution and readout stage.

In this case, the input light powers of the four photodiode are set to 1000, 600, 600, and 800 W/m^2 , while the weights are set to 20, 45, 70, and 70, respectively. With a fitting slope -0.00465955, the theoretical values of $U_{C1}-U_{C4}$ after the multiplication operation are 906.8, 874.2, 804.3, and 739.1 mV, respectively. The simulation results shown in Fig. 11 are 906.2, 874.0, 805.2, and 738.7 mV, which are consistent with the theoretical values.

B. MAC Operation Linearity Simulation

Fig. 12 shows the relationship between U_{out} and (a) the weight and (b) the input optical power. U_{out} is the readout voltage after the MAC operation. Linear fitting results of both figures show that the R^2 are all above 0.999. Results show that the proposed CIS architecture achieves high linearity and accuracy.

Fig. 13 shows the Differential Nonlinearity (DNL) and Integration Nonlinearity (INL) simulation results by the code density measurement. The simulated DNLs (INLs) in terms of the weight and the input light power are $+0.0755/-0.0206$ LSB ($+0.2334/-0.7242$ LSB) and $+0.0210/-0.0061$ LSB ($+0.3560/-1.1947$ LSB), respectively. The DNLs are all below 1 LSB, which means no missing codes.

C. Performance Analysis

The power consumption and performance comparison under different conditions are shown in Table II. The array size for all

situations is 1920×1080 , and the number of channels is 64. The calculation with 5×5 and 7×7 kernels is estimated by kernel splitting. The FoM (pJ/pixel/frame) presents the power consumed per frame (each channel counts once) per pixel. The computing efficiency (TOPS/w) shows the calculation amount divided by power consumption.

Table II shows that the designed sensor circuit's power consumption is related to the frame rate and the convolution kernel size. When the convolution kernel size keeps constant, the power consumption increases with the frame rate. In the same frame rate, the larger convolution kernel size leads to higher power consumption.

Computational efficiency (TOPS/w) changes remarkably in different conditions. The power consumption mainly comes from three parts: the convolution operation, the readout circuit, the column ADCs. Though the number of convolution operations and the number of readouts vary in the same proportion, the cost of ADCs remains unchanged, leading to increased computational efficiency when the computation increases. For example, with 60 FPS and stride is 2, the efficiency is 4.75 TOPS/w when the kernel size is 3×3 and is 6.76 TOPS/w when the kernel size is increased to 7×7 .

FoM (pJ/pixel/frame) increases with computation, but decreases with frame rate because of the same reason as the computational efficiency. It mainly represents the influence of convolution kernel size on power consumption. The increase of convolution kernel size will lead to a rise in computation and power consumption.

The change of stride will lead to a change in computation. If the stride is doubled, the computation and readout times will be reduced to a quarter, which leads to a decrease in power and FoM.

Table III compares the performance of this work with recent in-sensor computing works and shows our proposed architecture has a undeniable advantage in computing efficiency, which is about 3.6 times as higher as the state-of-the-art. As the proposed architecture integrates MAC operation with the pixel exposure, no additional analog computing circuit is used, which leads to extremely high efficiency.

D. Analysis of the Robustness

Operations in the analog domain are affected by undesirable factors such as noise and variations. In this section, we analyze the effects of these factors in detail.

1) *Device Variation*: As shown in Fig. 14, the schematic of the CIS computation parts can be simplified as a photodiode with a capacitor and two switches W_i and rd in each pixel. For an $r \times r$ convolution kernel, $r \times r$ pixels are connected to the same readout circuits, including a source follower transistor. After reset and exposure, V_{Ci} will be saved on C_i . When signal rd is set high, the voltages V_{Ci} connected in a kernel are averaged due to the charge sharing. In the ideal case, the readout voltage can be formulated as

$$V_{out} = \frac{\sum C_i V_{Ci}}{\sum C_i} - (V_{thi} + V_{od}) \quad (11)$$

where V_{thi} is the threshold of the source follower transistor in readout circuit and V_{od} is the over drive voltage. C_i is

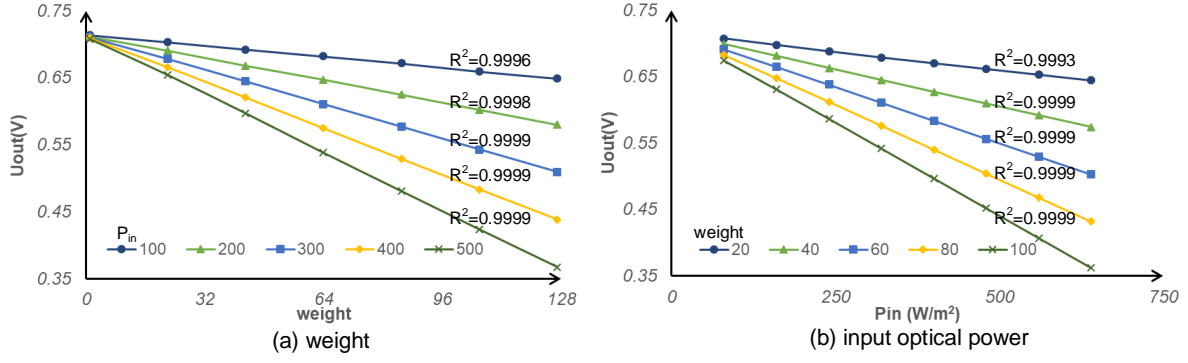


Fig. 12. Simulation of MAC operations. (a) Readout voltage for ADCs versus weight for different values of input optical power. (b) Readout voltage for ADCs versus input optical power for different values of weight.

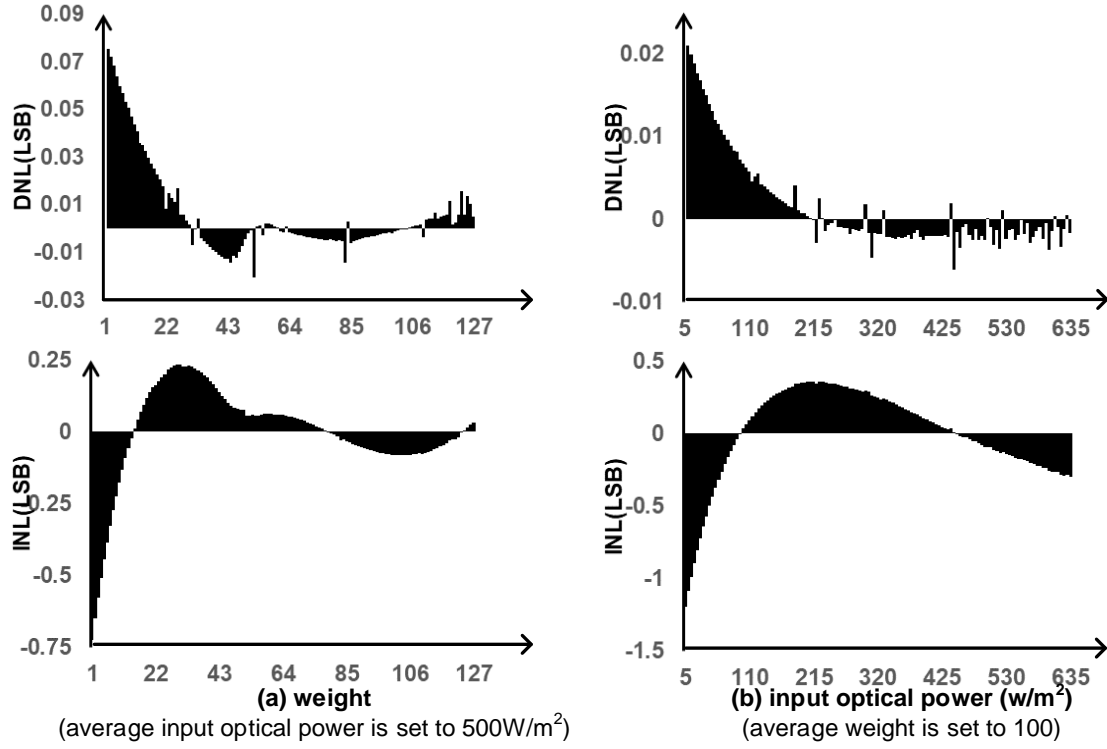


Fig. 13. The simulated DNL and INL in terms of (a) the weights, (b) the input optical power.

TABLE II

POWER CONSUMPTION ANALYSIS. THE AMOUNT OF THE MAC OPERATION IS CALCULATED ACCORDING TO THE GENERAL CALCULATION PRINCIPLE OF CONVOLUTION OPERATION, THAT IS, THE PRODUCT OF CONVOLUTION KERNEL SIZE r^2 , OUTPUT CHARACTERISTIC SIZE $\frac{HW}{s^2}$, NUMBER OF INPUT CHANNEL 3 (RGB), AND NUMBER OF OUTPUT CHANNELS n .

condition	Power(mW)	Efficiency(TOPS/w)	FoM (pJ/pixel/frame)
60FPS, 3×3 , $s=2$	22.62	4.75	2.85
120FPS, 3×3 , $s=2$	37.48	5.73	2.36
60FPS, 5×5 (splitting), $s=2$	48.34	6.18	6.06
60FPS, 5×5 (splitting), $s=4$	17.90	4.17	2.24
60FPS, 7×7 (splitting), $s=2$	86.47	6.76	10.85
60FPS, 7×7 (splitting), $s=4$	27.44	5.33	3.44

TABLE III
PERFORMANCE COMPARISON

	2017 ISSCC [12]	2019ASSCC [23]	2020TCASii [24]	2020TCASi [21]	this work
Process	90 nm/60 nm	180 nm	180 nm	180 nm	45 nm
Supply	3.3/2.9/1.8/1 V	0.5 V	1.8 V	2 V	1.1 V
Array Size	1296×976	128×128	32×32	32×32	1920×1080
Frame Rate	1000 fps	480 fps	1000 fps	100 fps	3840 fps
data/weight width	4 bit/NA	8 bit/4 bit	1 bit/1 bit	1 bit/1 bit	8 bit/8 bit
Feature	Spatial-Temporal processing	1st-layer CNN, ED,Blur,Sharpen	1st-layer BNN	1st-layer BNN	1st-layer CNN
Processing	Digital	Analog	Analog	Analog	Analog
Memory	Yes(Digital)	No	No	Yes(Analog)	No
Method	3D-stacked	switching-current-and-integration	dedicated SRAM	Kernel-Readout	pulse modulation
Power	363 mW	91 uW	12.16 uW	1.8 mW	22.62 mW
Computing Efficiency	0.386 TOPS/w	0.777 TOPS/w	1.32 TOPS/w	545.4 GOPS/w	4.75-6.76 TOPS/w
FoM(pJ/pixel/frame)	286.98	11.6	11.88	NA	2.85

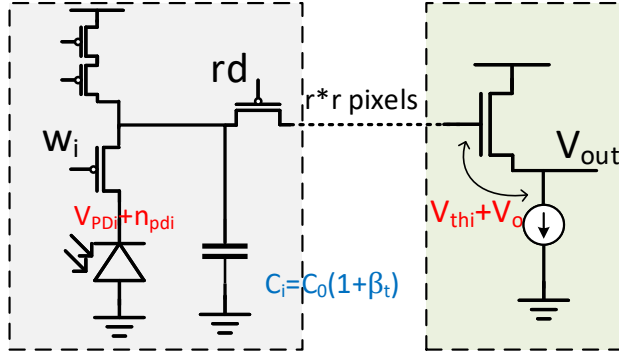


Fig. 14. Effects of variation, mismatch and noise. Red represents the voltage node influenced by the additive gaussian noise. Blue represents the threshold and the capacitance influenced by process variation and mismatch

the capacitor in each pixel. V_{out}^+ and V_{out}^- are the output voltages after charge sharing for positive and negative weights, respectively. As described in section III, the final output is obtained by the digital circuit subtracting the two voltages. The nominal capacitance of C_i is C_0 . Now we can illustrate the noise, variations, mismatch factors considered in our analysis.

Firstly, noise in the integrated circuits such as thermal noise, flicker noise, and environmental noise can be considered together as the additive Gaussian noise on the dynamic capacitance [11], as depicted in red in Fig. 14. Therefore,

$$V'_{Ci} = V_{Ci} + n_{Ci} = V_{PDi} + n_{pdi} + n_{ci} \quad (12)$$

where V_{PDi} and n_{pdi} are the value of V_{Ci} and the random noise, respectively. n_{ci} are the random noises on the capacitor. All noises follows the normal distribution $N(0, \sigma_{noise}^2)$.

Mismatch refers to the different deviations between different devices. It affect the threshold voltage of the source follower transistor and the capacitance of C_i . We can formulate it as

$$\begin{aligned} V_{thi} &= V_{th}(1 + \beta_{ti}) \\ C_i &= C_0(1 + \beta_{ci}) \end{aligned} \quad (13)$$

where β_{ti} and β_{ci} refer to the deviation of devices, both of which follow the normal distribution $N(0, \sigma_{mismatch}^2)$.

2) *Computation Error Analysis:* Given Eq. (11)-(13), the output V_{out} can be formulated as

$$V_{out} = V_{out}^+ - V_{out}^- = \frac{\sum (1 + \beta_{ci})(w_i x_i + n_{all})}{\sum (1 + \beta_{ci})} \quad (14)$$

where $n_{all} = n_{pdi}^+ + n_{ci}^+ - n_{pdi}^- - n_{ci}^-$. Because the four sums are independently distributed, n_{all} follows the normal distribution $N(0, 4\sigma_{noise}^2)$. β_{ci} follows the normal distribution with mean = 0, therefore Eq. (14) can be simplified as

$$V_{out} = \frac{\sum (1 + \beta_{ci})(w_i x_i + n_{all})}{4r^2} \quad (15)$$

Eq. (15) shows that (1) the impacts of all noise can be considered together as one random noise value n_{all} added to each pixel, which follows the normal distribution $N(0, 4\sigma_{noise}^2)$. (2) the mismatch across different capacitors in each pixel have the multiplicative factor $(1 + \beta_{ci})$ on the output data. (3) the impacts of devices' global process variation can be ignored because of the charge sharing operations and subtraction operations.

Compared with traditional design, the sharing operations have the extra benefit of increasing the SNR. The effect of the random additive noise in Eq. (15) can be expanded as

$$V_{out} = \frac{\sum w_i x_i}{4r^2} + \frac{\sum n_{all}}{4r^2} \quad (16)$$

As $\frac{\sum w_i x_i}{4r^2}$ is the desired output, $\frac{\sum n_{all}}{4r^2}$ is the additive noise. When the convolution kernel size is 3×3 , 9 pixels are connected, and each pixel has four photodiodes, so $4r^2 = 36$, which means $\sum n_{all}$ follows the normal distribution $N(0, 36\sigma^2)$. Then the noise and SNR can be calculated by

$$noise = E\left[\left(\frac{\sum n_{all}}{36}\right)^2\right] = \frac{1}{36^2} D(\sum n_{all}) = \frac{\sigma^2}{36} \quad (17)$$

$$SNR = \frac{power}{noise} = 36 \frac{power}{\sigma^2} \quad (18)$$

As shown in Eq. (18), the SNR is 36 times as high as traditional design, or a 15.6 dB increase. This means smaller

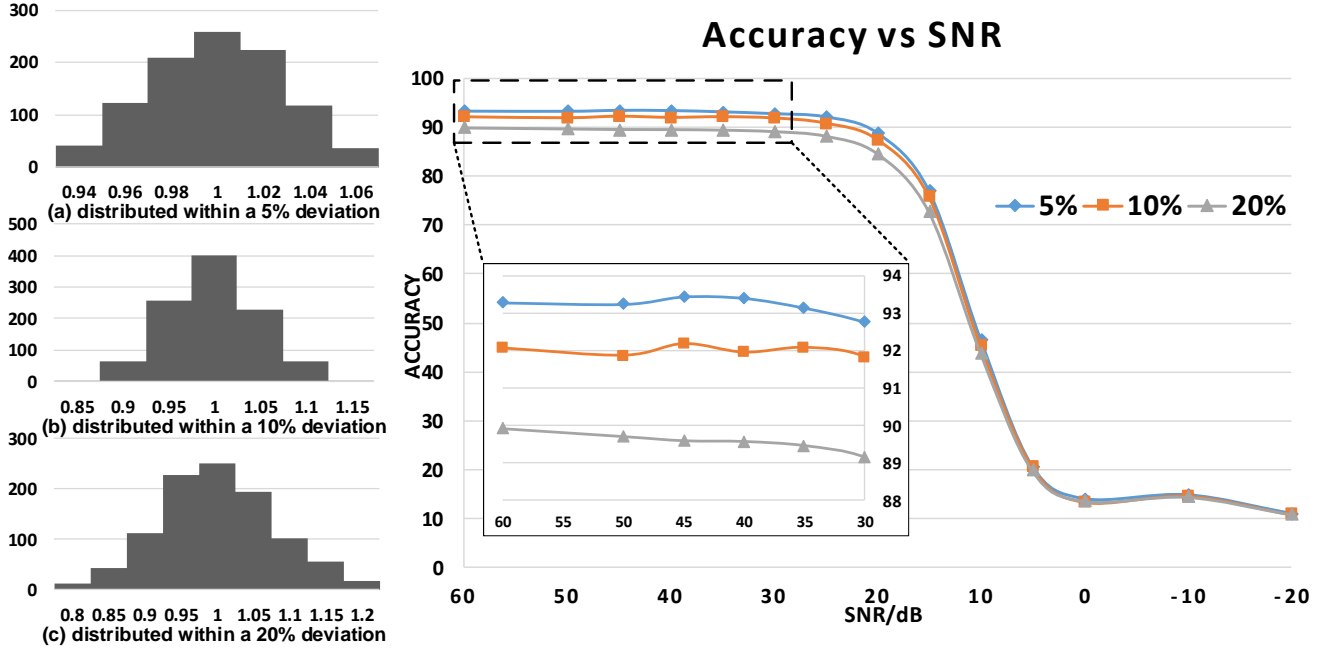


Fig. 15. Relationship between CNN accuracy and three types of disturbance.

capacitors are acceptable in our design, so the exposure time can be decreased, which contributed to a huge increase in frame rate to 3840 FPS.

3) *Algorithm Robustness*: As CNN algorithm is a neural network algorithm, its robustness is very high, and it can accept errors within a certain range of input data. Through network simulation with Cifar-10 [30] dataset and Resnet-18, the accuracy of CNN changes with SNR or mismatch as shown in Fig. 15. As the proposed CIS only support 1st-layer CNN, the rest calculation is achieved by software. Three different types of distributions of capacitors are used, and the distributions are shown in Fig. 15. The results showed little accuracy loss when SNR is more than 40 dB, as the typical SNR value for CIS is 40 dB - 60 dB[5].

Our proposed CIS circuit only support the 1-st layer of CNN, but is very important for the whole architecture's calculation. The quantization or pruning of the first layer of CNN usually lose a lot of accuracy, which makes it difficult to improve the performance. Due to the small number of input channels, DLAs' PEs are often not fully utilized for the first layer. Therefore, this design can greatly improve the computational efficiency of the subsequent DLAs, leading to much higher performance of the whole machine vision system.

V. CONCLUSION

In this work, a PIP architecture has been proposed to perform the first layer convolution operation of CNN. It supports a variety of different convolution kernel sizes and parameters. The simulation results have shown that our proposed scheme functions correctly with good linearity. In the case of the convolution kernel is 3×3 , step size is 2 and channel number is 64 at 60 frames and 1080P, the proposed architecture consumes

22.62 mW power, and have a computational efficiency up to 4.75 TOPS/w, which is about 3.6 times as higher as the state-of-the-art. It is very suitable for application scenarios with tight requirements on power consumption, such as daily monitoring and Internet of Things (IoT) terminal devices.

REFERENCES

- [1] S. Mane and S. Mangale, "Moving object detection and tracking using convolutional neural networks," in *2018 Second International Conference on Intelligent Computing and Control Systems (ICICCS)*, 2018, pp. 1809–1813.
- [2] C. Ding and D. Tao, "Trunk-branch ensemble convolutional neural networks for video-based face recognition," *IEEE Transactions on Pattern Analysis and Machine Intelligence*, vol. 40, no. 4, pp. 1002–1014, 2018.
- [3] L. Wu, K. Huang, H. Shen, and L. Gao, "Foreground-background parallel compression with residual encoding for surveillance video," *IEEE Transactions on Circuits and Systems for Video Technology*, pp. 1–1, 2020.
- [4] D. Wei, X. Xu, H. Shen, and K. Huang, "Gac-gan: A general method for appearance-controllable human video motion transfer," *IEEE Transactions on Multimedia*, pp. 1–1, 2020.
- [5] F. Zhou and Y. Chai, "Near-sensor and in-sensor computing," *Nature Electronics*, vol. 3, pp. 664–671, 2020.
- [6] M. T. Chung, C. L. Lee, C. Yin, and C. C. Hsieh, "A 0.5 v pwm cmos imager with 82 db dynamic range and 0.055% fixed-pattern-noise," *IEEE Journal of Solid-State Circuits*, vol. 48, no. 10, pp. 2522–2530, 2013.
- [7] X. Liu, M. Zhang, and J. Van der Spiegel, "A low-power multifunctional cmos sensor node for an electronic facade," *IEEE Transactions on Circuits and Systems I: Regular Papers*, vol. 61, no. 9, pp. 2550–2559, 2014.
- [8] O. Kumagai, A. Niwa, K. Hanzawa, H. Kato, and Y. Nitta, "A 1/4-inch 3.9mpixel low-power event-driven back-illuminated stacked cmos image sensor," in *2018 IEEE International Solid - State Circuits Conference - (ISSCC)*, 2018.
- [9] A. Y. Chiou and C. Hsieh, "An ulv pwm cmos imager with adaptive-multiple-sampling linear response, hdr imaging, and energy harvesting," *IEEE Journal of Solid-State Circuits*, vol. 54, no. 1, pp. 298–306, 2019.

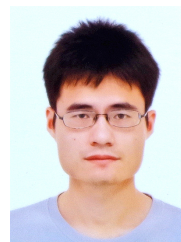
- [10] J. Choi, J. Shin, D. Kang, and D. Park, "Always-on cmos image sensor for mobile and wearable devices," *IEEE Journal of Solid-State Circuits*, vol. 51, no. 1, pp. 130–140, 2016.
- [11] A. Y. Chiou and C. Hsieh, "A 137 db dynamic range and 0.32 v self-powered cmos imager with energy harvesting pixels," *IEEE Journal of Solid-State Circuits*, vol. 51, no. 11, pp. 2769–2776, 2016.
- [12] T. Yamazaki, H. Katayama, S. Uehara, A. Nose, M. Kobayashi, S. Shida, M. Odahara, K. Takamiya, Y. Hisamatsu, S. Matsumoto, L. Miyashita, Y. Watanabe, T. Izawa, Y. Muramatsu, and M. Ishikawa, "4.9 a 1ms high-speed vision chip with 3d-stacked 140gops column-parallel pes for spatio-temporal image processing," in *2017 IEEE International Solid-State Circuits Conference (ISSCC)*, 2017, pp. 82–83.
- [13] M. F. Amir, D. Kim, J. Kung, D. Lie, S. Yalamanchili, and S. Mukhopadhyay, "Neurosensor: A 3d image sensor with integrated neural accelerator," in *2016 IEEE SOI-3D-Subthreshold Microelectronics Technology Unified Conference (S3S)*, 2016, pp. 1–2.
- [14] Z. Du, R. Fasthuber, T. Chen, P. Ienne, L. Li, T. Luo, X. Feng, Y. Chen, and O. Temam, "Shidiannao: Shifting vision processing closer to the sensor," in *2015 ACM/IEEE 42nd Annual International Symposium on Computer Architecture (ISCA)*, 2015, pp. 92–104.
- [15] Yunhui, Hou, Robert, LiKamWa, Lin, Zhong, Mia, Polansky, Julian, and Gao, "Redeye: Analog convnet image sensor architecture for continuous mobile vision," *Computer Architecture News*, 2016.
- [16] C. Xu, Y. Mo, G. Ren, W. Ma, X. Wang, W. Shi, J. Hou, K. Shao, H. Wang, P. Xiao, Z. Shao, X. Xie, X. Wang, and C. Yiu, "5.1 a stacked global-shutter cmos imager with sc-type hybrid-gs pixel and self-knee point calibration single frame hdr and on-chip binarization algorithm for smart vision applications," in *2019 IEEE International Solid-State Circuits Conference - (ISSCC)*, 2019, pp. 94–96.
- [17] L. Bose, J. Chen, S. J. Carey, P. Dudek, and W. Mayol-Cuevas, "Fully embedding fast convolutional networks on pixel processor arrays," 2020.
- [18] T. Hsu, Y. Chiu, W. Wei, Y. Lo, C. Lo, R. Liu, K. Tang, M. Chang, and C. Hsieh, "Ai edge devices using computing-in-memory and processing-in-sensor: From system to device," in *2019 IEEE International Electron Devices Meeting (IEDM)*, 2019, pp. 22.5.1–22.5.4.
- [19] A. El Gamal and H. Eltoukhy, "Cmos image sensors," *IEEE Circuits and Devices Magazine*, vol. 21, no. 3, pp. 6–20, 2005.
- [20] V. T. Lee, A. Alaghi, J. P. Hayes, V. Sathe, and L. Ceze, "Energy-efficient hybrid stochastic-binary neural networks for near-sensor computing," in *Design, Automation Test in Europe Conference Exhibition (DATE)*, 2017, pp. 13–18.
- [21] Z. Chen, H. Zhu, E. Ren, Z. Liu, K. Jia, L. Luo, X. Zhang, Q. Wei, F. Qiao, X. Liu, and H. Yang, "Processing near sensor architecture in mixed-signal domain with cmos image sensor of convolutional-kernel-readout method," *IEEE Transactions on Circuits and Systems I: Regular Papers*, vol. 67, no. 2, pp. 389–400, 2020.
- [22] T. Ma, K. Jia, X. Zhu, F. Qiao, Q. Wei, H. Zhao, X. Liu, and H. Yang, "An analog-memoryless near sensor computing architecture for always-on intelligent perception applications," in *2019 IEEE International Conference on Integrated Circuits, Technologies and Applications (ICTA)*, 2019, pp. 150–155.
- [23] T. Hsu, Y. Chen, T. Wen, W. Wei, Y. Chen, F. Chang, H. Kim, Q. Chen, B. Kim, R. Liu, C. Lo, K. Tang, M. Chang, and C. Hsieh, "A 0.5v real-time computational cmos image sensor with programmable kernel for always-on feature extraction," in *2019 IEEE Asian Solid-State Circuits Conference (A-SSCC)*, 2019, pp. 33–34.
- [24] H. Xu, Z. Li, N. Lin, Q. Wei, F. Qiao, X. Yin, and H. Yang, "Macsen: A processing-in-sensor architecture integrating mac operations into image sensor for ultra-low-power bnn-based intelligent visual perception," *IEEE Transactions on Circuits and Systems II: Express Briefs*, pp. 1–1, 2020.
- [25] L. Mennel, J. Symonowicz, S. Wachter, D. K. Polyushkin, and T. Mueller, "Ultrafast machine vision with 2d material neural network image sensors," *Nature*, vol. 579, no. 7797, pp. 62–66, 2020.
- [26] K. Bong, S. Choi, C. Kim, D. Han, and H. Yoo, "A low-power convolutional neural network face recognition processor and a cis integrated with always-on face detector," *IEEE Journal of Solid-State Circuits*, vol. 53, no. 1, pp. 115–123, 2018.
- [27] S. Wang, C.-Y. Wang, P. Wang, C. Wang, Z.-A. Li, C. Pan, Y. Dai, A. Gao, C. Liu, J. Liu, H. Yang, X. Liu, B. Cheng, K. Chen, Z. Wang, K. Watanabe, T. Taniguchi, S.-J. Liang, and F. Miao, "Networking retinomorphic sensor with memristive crossbar for brain-inspired visual perception," *National Science Review*, 07 2020, nwaal72. [Online]. Available: <https://doi.org/10.1093/nsr/nwaa172>
- [28] S. Zhang, K. Huang, and H. Shen, "A robust 8-bit non-volatile computing-in-memory core for low-power parallel mac operations,"

IEEE Transactions on Circuits and Systems I: Regular Papers, vol. 67, no. 6, pp. 1867–1880, 2020.

- [29] R. J. Perry and K. Arora, "Using pspice to simulate the photoresponse of ideal cmos integrated circuit photodiodes," in *Proceedings of SOUTH-EASTCON '96*, 1996, pp. 374–380.
- [30] A. Krizhevsky and G. Hinton, "Learning multiple layers of features from tiny images," *Handbook of Systemic Autoimmune Diseases*, vol. 1, no. 4, 2009.



Ruibing Song (Student Member, IEEE) received a bachelor's degree from the College of Electrical Engineering, Zhejiang University, in 2020. He is currently pursuing a master's degree at the College of Information Science & Electronic Engineering, Zhejiang University. He is interested in in-sensor computing and in-memory computing.



Kejie Huang (Senior Member, IEEE) received the Ph.D. degree from the Department of Electrical Engineering, National University of Singapore (NUS), Singapore, in 2014. He has been a Principal Investigator with the College of Information Science Electronic Engineering, Zhejiang University (ZJU), since 2016. Before joining ZJU, he has spent five years in the IC design industry, including Samsung and Xilinx, two years in the Data Storage Institute, Agency for Science Technology and Research (A*STAR), and another three years in Singapore University of Technology and Design (SUTD), Singapore. He has authored or coauthored more than 40 scientific articles in international peer-reviewed journals and conference proceedings. He holds four granted international patents, and another eight pending ones. His research interests include low power circuits and systems design using emerging non-volatile memories, architecture and circuit optimization for reconfigurable computing systems and neuromorphic systems, machine learning, and deep learning chip design. He currently serves as the Associate Editor of the IEEE TRANSACTIONS ON CIRCUITS AND SYSTEMS-PART II: EXPRESS BRIEFS.



Zongsheng Wang (Student Member, IEEE) received a bachelor's degree from the College of Electrical Engineering, Zhejiang University, in 2020. He is currently pursuing a master's degree at the College of Information Science & Electronic Engineering, Zhejiang University. He is interested in in-sensor computing, low power digital circuit design and deep learning accelerator.



Haibin Shen is currently a Professor with Zhejiang University, a member of the second level of 151 talents project of Zhejiang Province, and a member of the Key Team of Zhejiang Science and Technology Innovation. His research interests include learning algorithm, processor architecture, and modeling. His research achievement has been used by many authority organizations. He has published more than 100 papers in academic journals, and he has been granted more than 30 patents of invention. He was a recipient of the First Prize of Electronic Information

Science and Technology Award from the Chinese Institute of Electronics, and has won a second prize at the provincial level.